Special Issue Article

Institution of MECHANICAL ENGINEERS

Journal of ENGINEERING TRIBOLOGY

Proc IMechE Part J:
J Engineering Tribology
2015, Vol. 229(4) 547–556

DOI: 10.1177/1350650114545352
pij.sagepub.com

SAGE

The load-carrying capacity and friction coefficient of incompressible textured parallel slider bearings with surface roughness inside the texture features

Mingfeng Qiu and Bart Raeymaekers

Abstract

Surface texturing is used to increase hydrodynamic pressure and reduce friction and wear between parallel sliding surfaces in a variety of applications. The shape, geometry, and density of the patterned microtexture features play a key role in the tribological performance of such textured slider bearings. Lubrication models are used to predict the load-carrying capacity, friction coefficient, and volume flow rate of textured bearings, assuming a smooth surface and ideal shape of the texture features. However, experimental evidence shows that manufacturing techniques such as laser surface texturing only approach the ideal shape of the texture features. Moreover, the manufacturing process typically creates roughness inside the texture features. In this paper, we numerically evaluate the effect of roughness inside the texture features on the load-carrying capacity, friction coefficient, and volume flow rate of the textured parallel slider bearing. We consider the cases of sinusoidal roughness and isotropic random roughness with Gaussian distribution of surface heights and find that the effect of roughness inside the texture features on the bearing load-carrying capacity and friction coefficient increases with increasing roughness height and increasing wavelength of the roughness. In addition, the effect of sinusoidal roughness is larger than the effect of isotropic random roughness with Gaussian distribution of surface heights. We also find that the roughness inside the texture features has negligible impact on the volume flow rate of the textured bearing.

Keywords

Surface roughness, surface texturing, hydrodynamic lubrication, incompressible lubricant, parallel slider bearings

Date received: 20 November 2013; accepted: 23 June 2014

Introduction

Lubrication between two parallel sliding surfaces separated by a micro- or nanoscale gap is of critical importance for precision machinery and design of intricate and complex micro- and nanoscale sliding interfaces. Surface texturing is an effective way to reduce friction and wear between sliding surfaces separated by a thin compressible or incompressible lubricant film. A patterned microtexture on one of the sliding surfaces, usually implemented as a dense array of microsized concave features (“dimples”), increases the pressure in the lubricant, thereby increasing the load-carrying capacity of the bearing and reducing friction.[1,2] Several techniques have been used to manufacture microtexture patterns on engineering surfaces, including reactive ion etching,[3] abrasive jet machining,[4] LIGA,[5] and vibromechanical texturing.[6] Laser surface texturing (LST) may be the most widely used technique, likely because it is scalable to cover large surface areas.[7–9]

Lubrication models are crucial to optimize the geometry and pattern of the microtexture in terms of maximum load-carrying capacity,[10] minimum friction coefficient,[11] or other design objectives. Most models documented in the literature assume smooth bearing surfaces and ideal, smooth texture features, see e.g. studies by Qiu et al.,[10] Brizmer et al.,[12] Cupillard et al.,[13] Pascovici et al.,[14] and

Department of Mechanical Engineering, University of Utah, Salt Lake City, UT, USA

Corresponding author:
Bart Raeymaekers, Department of Mechanical Engineering, University of Utah, 50 S Central Campus Dr., MEB 2122, Salt Lake City, UT 84112, USA.
Email: bart.raeymaekers@utah.edu

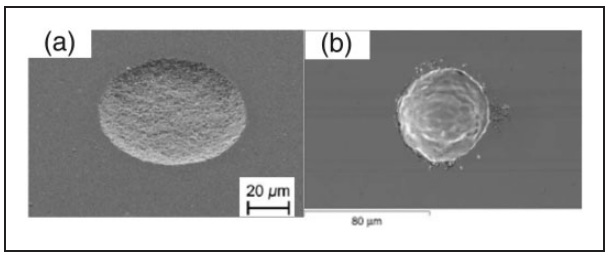

Figure 1. Waviness and roughness inside microsized surface texture features manufactured with (a) abrasive jet machining[4] and (b) LST.[8]

Rahmani et al.[15] However, assuming an ideal texture shape may not be realistic, as the texture features display waviness and roughness resulting from the manufacturing process, which can be non-negligible compared to the film thickness or the texture depth, and alter the bearing load-carrying capacity compared to what is predicted based on the ideal texture shape. Figure 1 shows typical microtexture features obtained with abrasive jet machining (Figure 1(a))[4] and LST (Figure 1(b)),[8] respectively. Surface topography inside the microsized texture features is clearly observed. Figure 2(a) shows a white light interferometer image of a circular dimple manufactured using LST on a cobalt chromium (CoCr) surface in the authors' lab. Figure 2(b) depicts a single two-dimensional (2D) trace through the centerline of the dimple, indicated in Figure 2(a). The surface topography of this trace is decomposed in low (waviness) and high (roughness) frequency components using digital signal processing with a cutoff frequency of $2.5 \times 10^4\,\mathrm{m}^{-1}$, as shown in Figure 2(c) and (d), respectively. The amplitude of the waviness is dominant over the amplitude of the roughness.

The effect of surface topography on the tribological characteristics of nominally smooth bearings (without microtexture) has been investigated since the 1960s. Early attempts have used the perturbation method to analytically calculate the effect of striated 2D sinusoidal roughness on the bearing load-carrying capacity.[16] Tzeng and Saibel[17] introduced a stochastic approach to study random roughness on a 2D inclined plane slider bearing and concluded that the load-carrying capacity is strongly affected by surface roughness. Other researchers have also used stochastic approaches.[18–24] An averaging method, based on flow factors compensating for three-dimensional (3D) random roughness effects in the traditional Reynolds equation, was pioneered by Patir and Cheng[25,26] and verified by Tripp.[27] They found that the roughness characteristics that affect the bearing load-carrying capacity include the roughness height compared to the film thickness, the ratio of roughness correlation lengths in different directions, and the ratio of the root mean square (RMS) roughness of the two sliding surfaces. Cavitation has also been considered, accounting for both inter-asperity cavitation and a macroscopic cavitation zone resulting from a diverging geometry of the bearing.[28,29] More recently, the homogenization

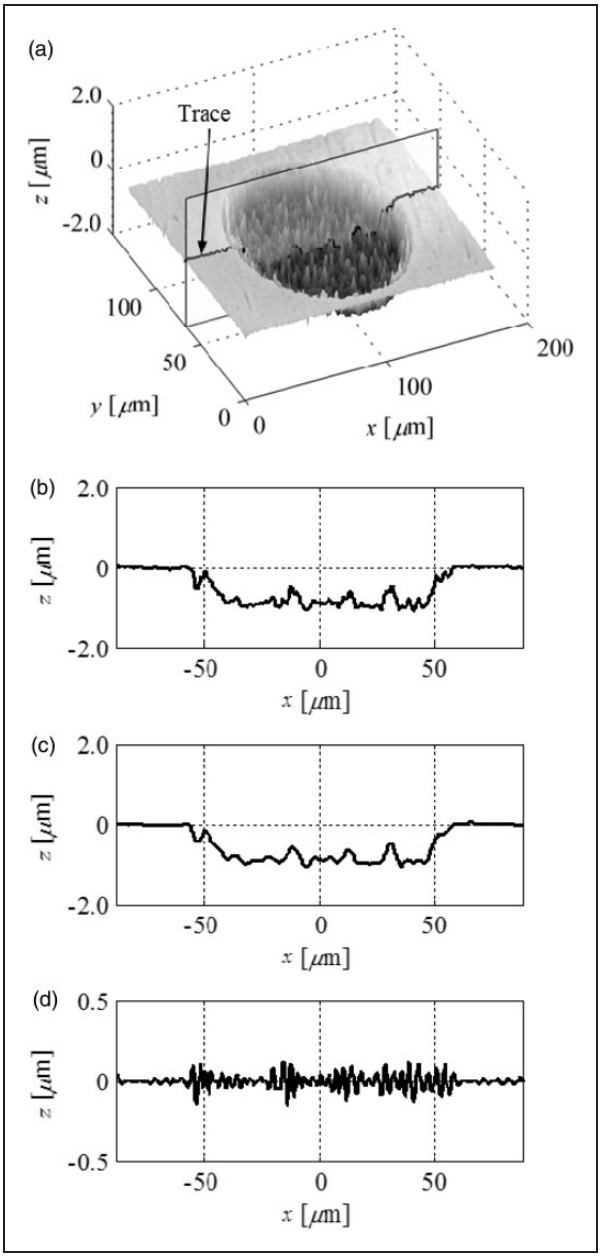

Figure 2. Circular dimple with $r_p = 50\,\mu\mathrm{m}$ and $h_p = 1\,\mu\mathrm{m}$, manufactured using LST on a CoCr surface. (a) white light interferometer image showing surface heights, (b) trace through the center of the dimple, (c) waviness portion of the trace, and (d) roughness portion of the trace.

method, used for the numerical solution of partial differential equations with rapidly changing coefficients,[30] has been implemented to solve lubrication problems that involve surface roughness.[31–36]

These studies have significantly improved the understanding of surface topography effects in lubrication films in nominally smooth bearings. However, no published studies seem to exist that document the effect of surface topography on textured bearing surfaces, independent of a specific application, and in particular taking into account the surface topography inside the texture features. This is of practical importance when designing and implementing textured bearings in

engineering applications. This paper attempts to fill this gap by quantifying the effect of surface topography inside the microtexture features on the load-carrying capacity, friction coefficient, and volume flow rate of a textured parallel slider bearing. To avoid ambiguity, the surface topography inside the texture features is referred to as roughness in this paper, without making distinction between waviness and roughness.

Model and numerical solution

Analytical model

Figure 3 shows a schematic of a textured parallel slider bearing. Figure 3(a) shows a top view, while Figure 3(b) displays a cross-sectional view through the center line of a column of circular dimples. The smooth surface moves with constant velocity U relative to the textured surface, separated by a liquid (incompressible) lubricant with constant viscosity. The textured surface is modeled as a column of 10 circular dimples, each centered in a square unit cell of length $2r_1$. Hydrodynamic lubrication is maintained and the inertia forces are negligible compared to the viscous forces as a result of the minute clearance between the sliding surfaces. No slip occurs between the liquid lubricant and the non-deformable solid surfaces. Hence, the pressure in the bearing as a function of the spacing is governed by the Reynolds equation, given in non-dimensional form as[12]

$$\frac{\partial}{\partial X}\left(H^3\frac{\partial P}{\partial X}\right)+\frac{\partial}{\partial Y}\left(H^3\frac{\partial P}{\partial Y}\right)=\frac{\lambda}{\delta^2}\frac{\partial H}{\partial X} \tag{1}$$

Here, $X=x/r_p$, $Y=y/r_p$ are the Cartesian coordinates normalized by the dimple radius r_p, with the origin as indicated in Figure 3. $H(X,Y)=h(x,y)/c$ is the lubricant film thickness normalized by the minimum bearing spacing c. $P(X,Y)=p(x,y)/p_0$ denotes the bearing gauge pressure normalized by the atmospheric pressure p_0. The flow parameter $\lambda=3\mu U/(2r_p p_0)$ and the non-dimensional bearing spacing $\delta=c/(2r_p)$ represent

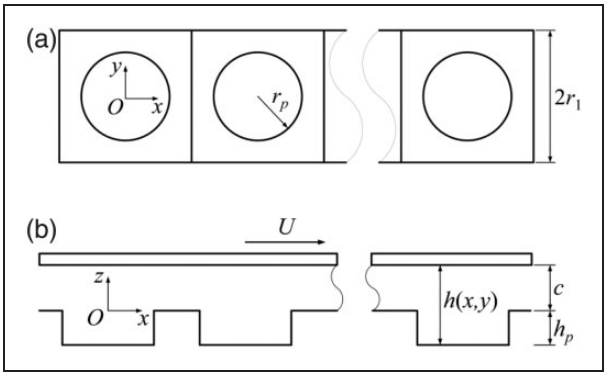

Figure 3. Schematic of a textured parallel slider bearing showing (a) the top view of the bearing and (b) the cross-sectional view of the bearing.

the operating conditions of the bearing. μ is the dynamic viscosity of the lubricant. The Reynolds cavitation boundary condition is enforced with the cavitation pressure equal to the atmospheric pressure,[37] which is discussed in more detail in the "Validity of the Reynolds equation" section. Additionally, atmospheric pressure is applied at the inlet and outlet of the bearing in the stream-wise direction (x-direction) and symmetry boundary conditions are applied in the span-wise direction (y-direction), representing the presence of adjacent columns of dimples. Thus

$$\begin{aligned}&P\left(X=-\frac{r_1}{r_p},Y\right)=P\left(X=(2N-1)\frac{r_1}{r_p},Y\right)=0\\&\frac{\partial P}{\partial Y}\left(X,Y=-\frac{r_1}{r_p}\right)=\frac{\partial P}{\partial Y}\left(X,Y=\frac{r_1}{r_p}\right)=0\end{aligned} \tag{2}$$

with $N=10$, the number of dimples used in the numerical model. The microtexture geometry is described by the texture aspect ratio $\varepsilon=h_p/(2r_p)$, defined as the ratio of texture depth h_p and texture diameter $2r_p$, and the texture density $S_p=\pi {r_p}^2/(4{r_1}^2)$, defined as the ratio of the bearing surface covered by the microtexture and the total bearing area. The non-dimensional bearing load-carrying capacity per unit area, W, is the integral of the local non-dimensional bearing pressure within the solution domain Ω divided by the entire non-dimensional bearing area S. The bearing area is non-dimensionalized with ${r_p}^2$, since both horizontal dimensions (X and Y) are non-dimensionalized with r_p. Thus

$$W=\frac{1}{S}\int\int_{\Omega}P\mathrm{d}\Omega \tag{3}$$

The shear stress in the sliding direction (x-direction) on the smooth surface τ_{zx} is derived from the lubricant flow velocity in the sliding direction u,[37] i.e. $\tau_{zx}=\mu(\partial u/\partial z)$. Non-dimensionalized with the atmospheric pressure p_0, the non-dimensional shear stress T_{ZX} is expressed as

$$T_{ZX}=\delta\frac{\partial P}{\partial X}H+\frac{\lambda}{3\delta}\frac{1}{H} \tag{4}$$

The non-dimensional friction force F_f is the integral of the shear stress T_{ZX} over the solution domain Ω, i.e.

$$F_f=\delta\int\int_{\Omega}H\frac{\partial P}{\partial X}\mathrm{d}\Omega+\frac{\lambda}{3\delta}\int\int_{\Omega}\frac{1}{H}\mathrm{d}\Omega \tag{5}$$

The bearing friction coefficient f is defined as the ratio of the non-dimensional friction force F_f and the non-dimensional bearing load-carrying capacity WS, i.e.

$$f=\frac{F_f}{WS} \tag{6}$$

In addition, the volume flow rate of the bearing, q, is defined as the volume of lubricant passing through any y-z cross-section per unit time. Hence, the non-dimensional volume flow rate $Q = q/(Ur_pc/2)$ is written as

$$Q = -\frac{\delta^2}{\lambda}\int_{-r_1/r_p}^{r_1/r_p} H^3(-r_1/r_p, Y)\frac{\partial P}{\partial X}(-r_1/r_p, Y)\mathrm{d}Y + \int_{-r_1/r_p}^{r_1/r_p} H(-r_1/r_p, Y)\mathrm{d}Y \tag{7}$$

where the integration is performed on the inlet cross-section of the bearing ($X = -r_1/r_p$, in the coordinate system of Figure 3).

Roughness inside the dimple

We have considered two types of roughness inside the dimples; 2D sinusoidal surface roughness, oriented transverse to the stream-wise direction, which mimics the anisotropic waviness that often results from LST, and isotropic 3D random roughness with Gaussian distribution of surface heights.[38]

The surface height of the sinusoidal roughness R in each dimple is described as

$$R = A\sin(\pi kX + \varphi) \tag{8}$$

where X is the non-dimensional x-coordinate, with its origin located in the center of the dimple. φ is the phase, which is defined as the shift of the 2D sinusoidal roughness in the stream-wise direction. A is the amplitude of the sine wave, and k is the wave number, denoting the number of complete wavelengths within the distance of one dimple diameter. We choose k to be an integer such that the mean roughness height is always 0. The RMS roughness is expressed as

$$\sigma = \sqrt{\frac{1}{2}\int_{-1}^{1} R^2\mathrm{d}X} = \frac{|A|}{\sqrt{2}} \tag{9}$$

Normalizing the RMS roughness with respect to the texture depth h_p yields

$$\sigma^* = \frac{|A|}{\sqrt{2}h_p} \tag{10}$$

The 3D isotropic random roughness with Gaussian distribution of surface heights is numerically generated using the method by Hu and Tonder,[39] which is based on filtering an array of uniformly distributed random numbers with a circularly symmetric low-pass filter with cutoff frequency f_c. Since the exact autocorrelation function is not explicitly specified in this method, the parameters to control the roughness are limited to the non-dimensional RMS roughness σ^* and the normalized frequency α, defined as the ratio of the cutoff frequency f_c and the sampling frequency f_s of the low-pass filter. Figure 4(a) shows an example of the 2D sinusoidal roughness and Figure 4(b) shows an example of the 3D isotropic random roughness with Gaussian distribution of surface heights inside a single dimple.

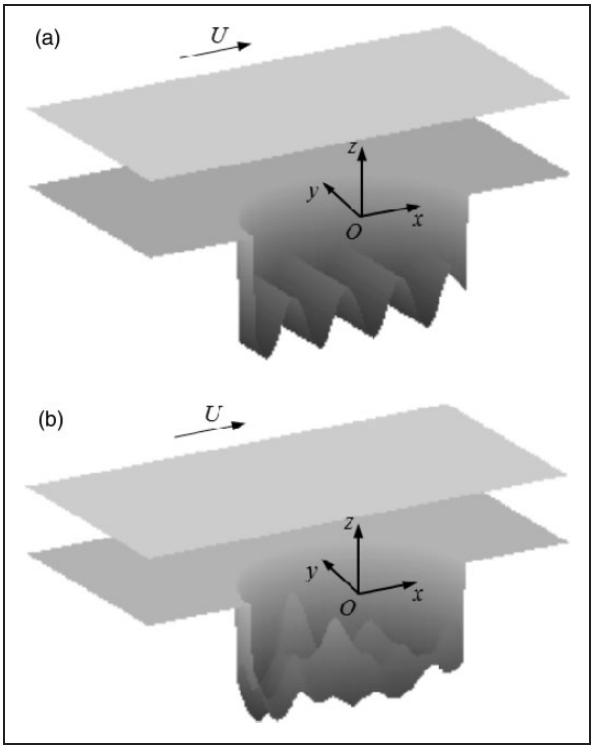

Figure 4. Typical examples of roughness inside the dimples (spacing between the sliding surfaces not drawn to scale for clarity). (a) 2D sinusoidal roughness and (b) 3D isotropic random roughness with Gaussian distribution of surface heights.

Numerical method

A central finite difference scheme on a rectangular staggered grid[40] is used to iteratively solve equation (1) for the local bearing pressure $P(X,Y)$, using an over-relaxation factor of 1.9. We have used 289 grid points inside each dimple in both the stream- and span-wise directions. The non-uniform grid is approximately six times denser inside than outside the dimples to resolve the steep pressure gradients inside the dimples. A gradual transition of the grid size is used to improve numerical accuracy.[41] Convergence is obtained to within 10^{-6} relative difference of the pressure solution between successive iterations, using the L_1 vector norm.[42] Further refinement of the grid does not change the solution by more than 0.5%.

Numerical experiments with this model indicate that the bearing operating conditions (λ and δ) and the texture geometry (ε and S_p) minimally change the effect of the roughness on the bearing load-carrying

capacity. Hence, we have maintained constant texture geometry and bearing operating conditions throughout this study. The texture diameter $2r_p = 100\,\mu m$ and texture depth $h_p = 1\,\mu m$, i.e. $\varepsilon = 0.010$, and the texture density $S_p = 0.20$. We have selected these texture parameters similar to the geometry that maximizes the load-carrying capacity,[43] but we also consider manufacturability of the texture. While $\varepsilon < 0.010$ may increase the bearing load-carrying capacity, it is difficult to reliably manufacture such shallow dimple geometries using LST. Water is used as lubricant with $\mu = 1.0 \times 10^{-3}$ Pa·s. The sliding velocity $U = 10$ m/s and the minimum bearing spacing is maintained at 0.1 μm. These parameters are relevant to applications such as thrust bearings and mechanical seals.[12,43] The corresponding non-dimensional parameters are $\varepsilon = 0.01$, $S_p = 0.20$, $\delta = 0.001$, and $\lambda = 3.0 \times 10^{-3}$.

The parameters that characterize the roughness $0 \leqslant \sigma^* \leqslant 0.2$, $2 \leqslant k \leqslant 32$, $0 \leqslant \varphi \leqslant 2\pi$ are chosen such that the Reynolds equation (equation (1)) remains valid (see also the "Validity of the Reynolds equation" section). Also, the spatial frequency range (wave number k) is in line with the dominant low-frequency components observed inside dimples manufactured with LST (Figure 2). Similarly, the 3D isotropic random roughness with Gaussian distribution of surface heights is evaluated with $0 \leqslant \sigma^* \leqslant 0.2$ and $0.01 \leqslant \alpha \leqslant 0.10$. Since a stochastic process is employed to create the Gaussian distribution of surface heights, the random roughness is different each time it is generated using the same σ^* and α. Hence, it is necessary to average the results over multiple simulations with different random roughness of the same σ^* and α. From the point of view of statistics, converging to the mean values of the calculated quantities requires a large number of such simulations. On the other hand, the high computational cost poses a limit to the number of simulations that can be performed. Thus, for each combination of σ^* and α, the calculations are averaged over 10 simulations. In each simulation, a new random roughness inside the dimples is generated. The bearing load-carrying capacity, friction coefficient, and volume flow rate are compared to those of the textured bearings with ideal texture shape, i.e. without surface roughness inside the dimples.

Simulation results and discussion

Sinusoidal roughness

Figure 5 shows the deviation of the bearing load-carrying capacity and friction coefficient for textured bearings with 2D sinusoidal roughness inside the dimples, relative to that of textured bearings with ideal dimple shapes. The inset images visualize the roughness inside the dimples for three example cases. The results are shown for different combinations of wave number k and non-dimensional RMS roughness height σ^*, and for $\varphi = 0$. From Figure 5(a), we observe that the 2D transverse sinusoidal roughness mostly increases the bearing load-carrying capacity compared to idealized textured bearings without roughness inside the dimples. It is noted that the roughness features with parameters (σ^*, k) below the 0 contour line in Figure 5(a) cause a relative deviation between 0 and −0.003 in bearing load-carrying capacity compared to the ideal dimple shape. Hence, the effect of roughness in this region is negligible. The deviation between the cases with and without roughness inside the dimples increases with increasing σ^* and can exceed 10% when σ exceeds 15% of the texture depth ($\sigma^* > 0.15$). Additionally, the deviation between both models decreases with increasing wave number k, i.e. with decreasing wavelength of the roughness. For small values of k, the roughness

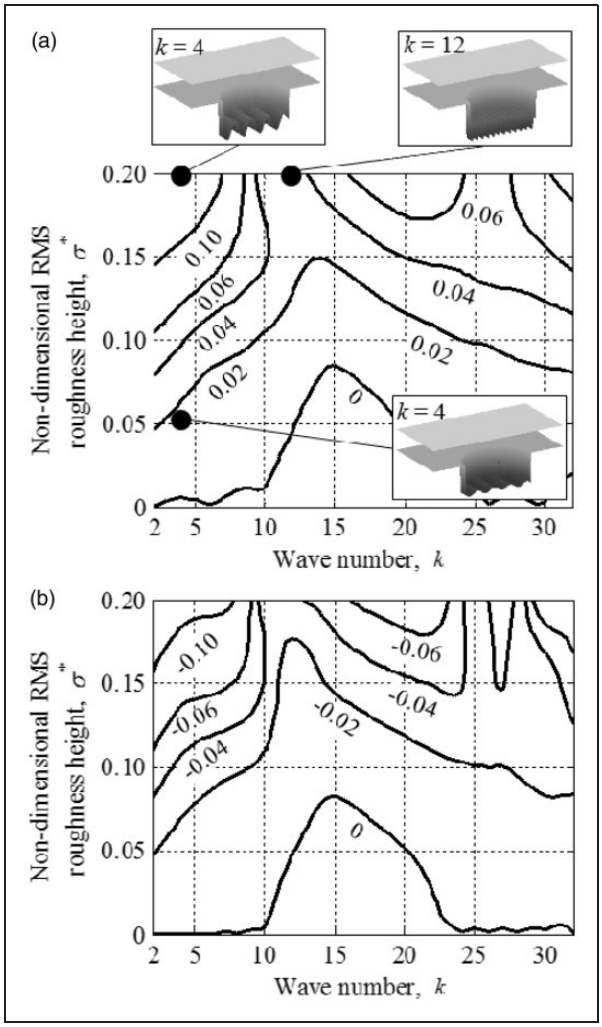

Figure 5. Deviation of the bearing load-carrying capacity and friction coefficient of textured bearings with 2D transverse sinusoidal roughness and those with an ideal dimple shape, as a function of wave number k and non-dimensional RMS roughness height σ^*. $\varphi = 0$, $\varepsilon = 0.01$, $S_p = 0.20$, $\delta = 0.001$, and $\lambda = 3.0 \times 10^{-3}$. (a) load-carrying capacity and (b) friction coefficient.
RMS: root mean square.

features have a long wavelength. This acts as secondary microtexture inside the original dimples. In contrast, with increasing k and decreasing wavelength of the roughness, the effect of this secondary texture on the local bearing pressure decreases. Figure 5(b) shows that the friction coefficient results correlate well with the load-carrying capacity results. As the roughness increases, the bearing load-carrying capacity increases while the friction coefficient decreases by approximately the same percentage, i.e. the friction force is only slightly affected. We have also calculated the deviation of the volume flow rate between textured bearings with 2D transverse sinusoidal roughness and those with an ideal dimple shape but found this relative deviation to be within the range of -1×10^{-3} to 1×10^{-3}. Hence, the effect on the volume flow rate of the bearing is negligible.

Figure 6 illustrates this in more detail and shows the local pressure along the center line of the bearing inside a single dimple (fifth dimple in the column of $N = 10$ dimples), for 2D sinusoidal roughness of different wave numbers, and for $\sigma^* = 0.20$. The local pressure of the bearing with an ideal dimple shape is shown in bold. A schematic dimple cross-section is shown for reference. We observe that the magnitude of the ripples in the local pressure caused by the roughness decreases to an asymptotic limit with decreasing wavelength (increasing k) of the roughness inside the dimple. This asymptote is close to the reference local pressure of the textured bearing with no surface roughness inside the dimples.

Figure 7 shows the deviation of the load-carrying capacity and friction coefficient for textured bearings with and without 2D sinusoidal roughness inside the dimples, as a function of φ and k, for $\sigma^* = 0.15$. For constant k, the deviation of the bearing load-carrying capacity depends strongly on the phase φ of the 2D sinusoidal roughness, in particular for small wave numbers (Figure 7(a)). For example, if $k = 2$, the deviation varies between 0% and 10% as a function of φ. Since long wavelength roughness features have a larger effect on the bearing load-carrying capacity (see Figure 5), the effect of the phase increases with increasing wavelength (decreasing k). In addition, for a constant change in the phase, $\Delta\varphi$, the linear displacement of the sinusoidal roughness features in the dimple increases with decreasing k, thus having a stronger effect on the bearing load-carrying capacity. Similarly, the deviation of the bearing friction coeffcient closely follows that of the load-carrying capacity (Figure 7(b)). In addition, the deviation of the volume flow rate is again found to be neglegible, with absolute values smaller than 1×10^{-3}.

Random roughness with Gaussian distribution of surface heights

Figure 8 shows the deviation of the bearing load-carrying capacity and friction coefficient for textured

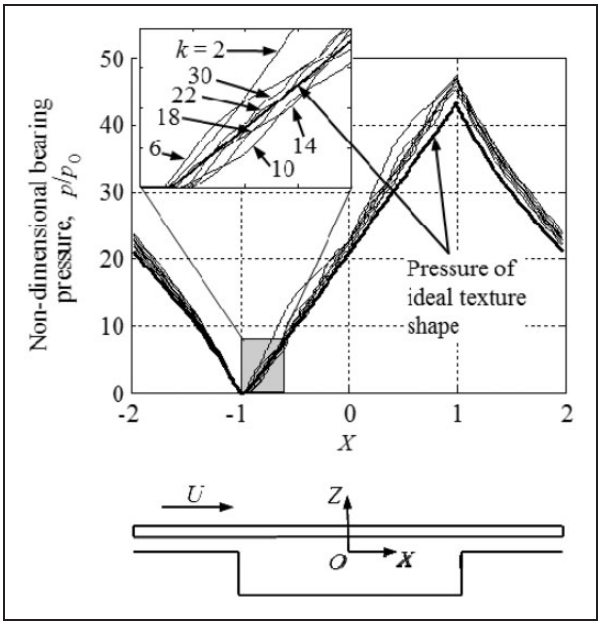

Figure 6. Local pressure along the center line of the fifth unit cell of the textured bearing with 2D transverse sinusoidal roughness inside the dimples, for different wave numbers. $\varphi = 0$, $\sigma^* = 0.20$. $\varepsilon = 0.01$, $S_p = 0.20$, $\delta = 0.001$, and $\lambda = 3.0 \times 10^{-3}$. The bold line indicates the reference local pressure of the bearing without roughness inside the dimples. The dimple cross-section is shown for reference.

bearings with 3D isotropic random roughness with Gaussian distribution of surface heights inside the dimples, relative to that of textured bearings with ideal dimple shapes. The inset images visualize the roughness inside the dimples for three example cases. The results are shown for different combinations of RMS roughness height σ^* and normalized frequency α. Each data point represents the average of 10 simulations. For each simulation, a new 3D isotropic random roughness with Gaussian distribution of surface heights is used inside the dimples. Similar to the results for the 2D sinusoidal roughness, we observe that the deviation between the bearing load-carrying capacity for the cases with and without roughness inside the dimples increases with increasing σ^*. However, the presence of the 3D isotropic random roughness with Gaussian distribution of surface heights slightly decreases the bearing load-carrying capacity. Figure 8(a) shows that the deviation of the bearing load-carrying capacity for the cases with and without random roughness is less than 2% throughout the range of parameters considered. In addition, the deviation of the bearing load-carrying capacity increases with decreasing normalized frequency α. Without averaging the bearing load-carrying capacity over 10 simulations, the result varies significantly for individual simulations with small α. A low value of α, corresponding to a low value of k for 2D sinusoidal roughness, results in a surface that is dominated by long wavelength roughness features, which have a

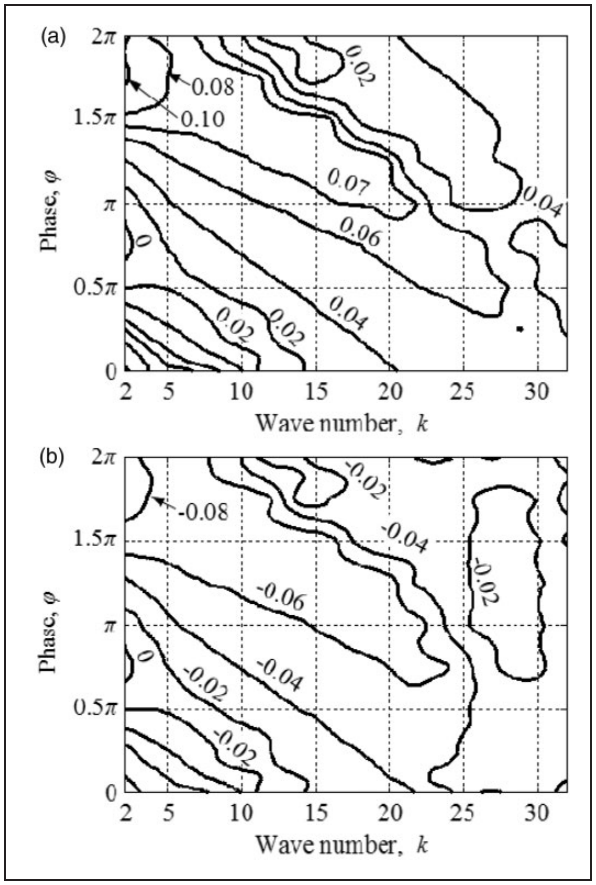

Figure 7. Deviation of the bearing load-carrying capacity and friction coefficient of textured bearings with 2D transverse sinusoidal roughness and those with an ideal texture shape as a function of wave number k and phase φ values. $\sigma^* = 0.15$. $\varepsilon = 0.01$, $S_p = 0.20$, $\delta = 0.001$, and $\lambda = 3.0 \times 10^{-3}$. (a) load-carrying capacity and (b) friction coefficient.

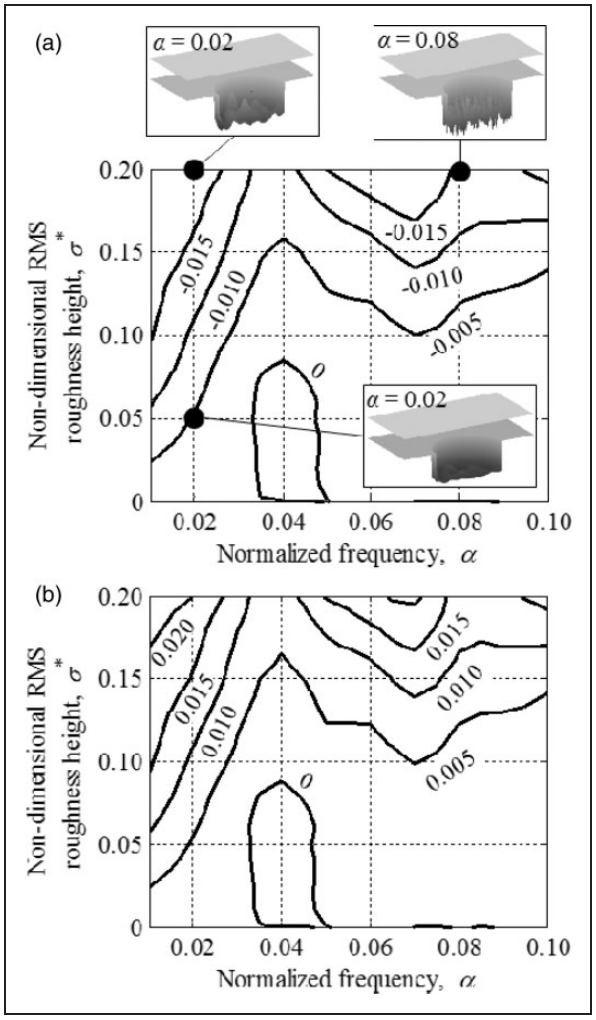

Figure 8. Deviation of the bearing load-carrying capacity and friction coefficient of textured bearings with 3D isotropic random roughness with Gaussian distribution of surface heights and those with an ideal texture shape, as a function of RMS roughness height σ^* and normalized frequency α. $\varepsilon = 0.01$, $S_p = 0.20$, $\delta = 0.001$, and $\lambda = 3.0 \times 10^{-3}$. (a) load-carrying capacity and (b) friction coefficient.
RMS: root mean square.

larger effect on the bearing load-carrying capacity than short wavelength roughness features, and act as a secondary texture inside the microtexture. Figure 8(b) shows that the deviation of the bearing friction coefficient is also closely related to the deviation of the bearing load-carrying capacity, similar to observations made for textured bearings with 2D transverse sinusoidal roughness inside the dimples. In addition, the deviation of the volume flow rate of the bearing can also be neglected, with absolute values less than 1×10^{-4}.

Validity of the Reynolds equation

The model used in this work only considers roughness inside the texture features. Figure 2 illustrates that the surface roughness in the non-textured regions of the bearing, which can be polished, is negligible compared to that inside the dimple. Dividing the bearing domain into regions with roughness (inside the dimples) and without roughness (outside the dimples) makes it difficult to apply the numerical techniques outlined in the introduction. In addition, most of these techniques do not take cavitation into account.[16–20,22–26] Hence, we use the Reynolds equation to simulate the local bearing pressure. The surface topography inside the texture features is described deterministically, similar to what has been done in studies involving complex fluid-solid structure interaction.[44–46] We use a non-uniform grid to resolve the surface topography inside the texture features while maintaining computational efficiency.

The Reynolds equation is valid when the wavelength of roughness features is large and the roughness height is small, compared to the mean film thickness (referred to as Reynolds roughness).[47–49] However, the Stokes equations must be used if these assumptions are violated (referred to as Stokes roughness).[48–52] Elrod[47] suggests that the limit for the ratio of the mean film thickness to the wavelength of the surface topography beyond which the Reynolds equation is no longer valid, is 0.2, while Bayada and

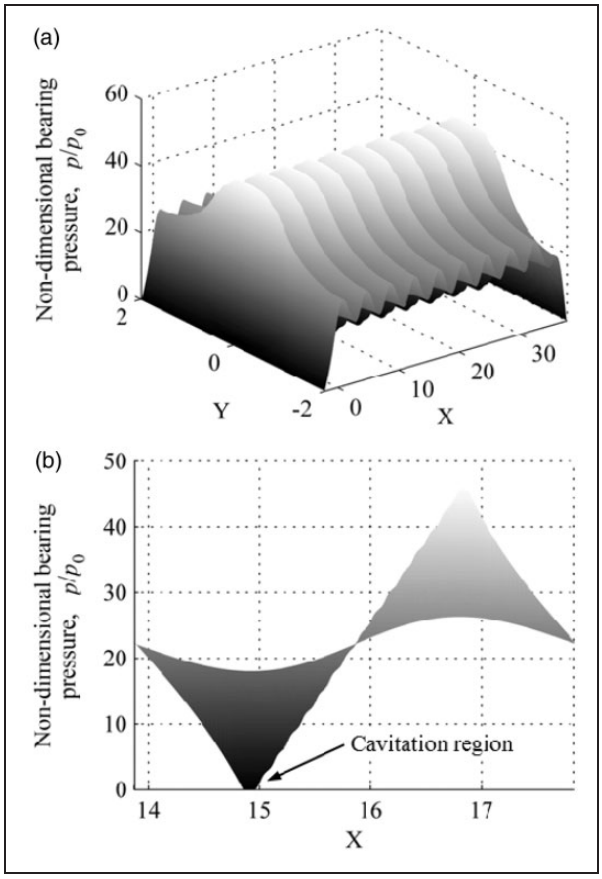

Figure 9. Local pressure in the textured parallel slider bearing with 2D transverse sinusoidal roughness inside the dimples. $\varphi = 0$, $\sigma^* = 0.20$, $k = 16$. $\varepsilon = 0.01$, $S_p = 0.20$, $\delta = 0.001$, and $\lambda = 3.0 \times 10^{-3}$. (a) solution for a row of 10 dimples and (b) solution along the centerline of the fifth dimple cell in the x-direction.

Faure[32] suggest it to be 1. The smallest wavelength of the roughness features that we have considered in this study is approximately 30 times larger than the minimum bearing spacing outside the dimples and three times larger than the texture depth. On the other hand, the maximum RMS roughness height is only 20% of the texture depth (see the "Numerical Method" section). Therefore, the ratio of the mean film thickness to the surface topography wavelength is still considered to be sufficiently small. It has also been demonstrated that even when the Reynolds equation is no longer justified to predict the local bearing pressure, the calculation of the load-carrying capacity of the textured bearing is still accurate.[53] It is pointed out that extrapolating the conclusions to roughness features with shorter wavelengths than what is considered in this study should be performed with caution. The use of the Reynolds equation may no longer be justified as the wavelength of the roughness features is reduced further. However, experimental data (Figure 2) shows that the amplitude of short wavelength roughness features is small and, thus, it may only have limited influence on the conclusions.

It has been shown in other studies[54,55] that the Reynolds cavitation boundary condition may be inaccurate in predicting the local pressure and friction coefficient in textured bearings, due to the unrealistically small cavitation area and excessive pressure generation. Figure 9(a) shows the local pressure in the textured parallel slider bearing with 2D transverse sinusoidal roughness inside the dimples with $\varphi = 0$, $\sigma^* = 0.20$, $k = 16$. Figure 9(b) shows the local pressure along the centerline of the fifth dimple cell in the x-direction. The cavitation area is small compared to the size of the dimple cell, similar to results of other studies[54,55] that use the Reynolds cavitation model. However, the deviation of load-carrying capacity, friction coefficient, and volume flow rate of bearings with or without roughness inside the dimples, both simulated using the Reynolds cavitation condition, is very limited in magnitude.

Friction increases lubricant temperature, which in turn reduces lubricant viscosity and, thus, the bearing load-carrying capacity. Our results predict that the 2D transverse sinusoidal roughness will increase the bearing load-carrying capacity, decrease the friction coefficient, which could also reduce lubricant heating.

Conclusions

We have investigated the effect of roughness inside the texture features of a textured parallel slider bearing on the bearing load-carrying capacity, friction coefficient, and volume flow rate. We conclude that the effect of roughness inside the texture features on the bearing load-carrying capacity increases with increasing roughness height and increasing wavelength of the roughness. The deviation between the bearing load-carrying capacity with and without taking into account the roughness inside the texture features may be as high as 10% in the case of sinusoidal roughness with σ^* in excess of 15% of the depth of the texture features. When considering isotropic random roughness with Gaussian distribution of asperity heights, the effect of roughness on the bearing load-carrying capacity is found to be negligible. The deviation of the bearing friction coefficient is closely related to the deviation of the load-carrying capacity. The effect of roughness on the volume flow rate of the bearings can always be neglected.

Conflict of interest

None declared.

Funding

This work is partially funded through NSF award #1227869 and NIH award #1R41AR064095-01.

References

1. Kovalchenko A, Ajayi O, Erdemir A, et al. The effect of laser texturing on transitions in lubrication regimes during unidirectional sliding contact. *Tribol Int* 2005; 38: 219–225.

2. Galda L, Pawlus P and Sep J. Dimple shape and distribution effect on characteristics of stribeck curve. *Tribol Int* 2009; 42: 1505–1512.
3. Wang X and Kato K. Improving the anti-seizure ability of SiC seal in water with RIE texturing. *Tribol Lett* 2003; 14: 275–280.
4. Wakuda M, Yamauchi Y, Kanzaki S, et al. Effect of surface texturing on friction reduction between ceramic and steel materials under lubricated sliding contact. *Wear* 2003; 254: 356–363.
5. Stephens L, Siripuram R, Hayden M, et al. Deterministic micro asperities on bearings and seals using a modified LIGA process. *J Eng Gas Turb Power* 2004; 126: 147–154.
6. Greco A, Raphaelson S, Ehmann K, et al. Surface texturing on tribological interfaces using the vibromechanical texturing method. *J Manuf Sci E-T ASME* 2009; 131: 1–8.
7. Duffet G, Sallamand P and Vannes A. Improvement in friction by cs Nd:YAG laser surface treatment on cast iron cylindrical bore. *App Surf Sci* 2003; 205: 289–296.
8. Vilhena L, Sedlacek M, Podgornik B, et al. Surface texturing by pulsed Nd:YAG laser. *Tribol Int* 2009; 42: 1496–1504.
9. Etsion I. State of the art in laser surface texturing. *J Tribol-T ASME* 2005; 127: 248–253.
10. Qiu M, Delic A and Raeymaekers B. The effect of texture shape on the load-carrying capacity of gas-lubricated parallel slider bearings. *Tribol Lett* 2012; 48: 315–327.
11. Qiu M, Minson B and Raeymaekers B. The effect of texture shape on the friction coefficient and stiffness of gas-lubricated parallel slider bearings. *Tribol Int* 2013; 67: 278–288.
12. Brizmer V, Kligerman Y and Etsion I. A laser surface textured parallel thrust bearing. *Tribol T* 2003; 46: 397–403.
13. Cupillard S, Glavatskih S and Cervantes MJ. Computational fluid dynamics analysis of a journal bearing with surface texturing. *Proc IMechE, Part J: J Engineering Tribology* 2008; 222: 97–107.
14. Pascovici MD, Cicone T, Fillon M, et al. Analytical investigation of a partially textured parallel slider. *Proc IMechE, Part J: J Engineering Tribology* 2009; 223: 151–158.
15. Rahmani R, Shirvani A and Shirvani H. Optimization of partially textured parallel thrust bearings with square-shaped micro-dimples. *Tribol T* 2007; 50: 401–406.
16. Burton R. Effects of two-dimensional, sinusoidal roughness on the load support characteristics of a lubricant film. *J Basic Eng-T ASME* 1963; 85: 258–264.
17. Tzeng S and Saibel E. Surface roughness effect on slider bearing lubrication. *ASLE Trans* 1967; 10: 334–348.
18. Christensen H. Stochastic models for hydrodynamic lubrication of rough surfaces. *Proc Inst Mech Eng* 1969; 184: 1013–1026.
19. Christensen H and Tonder K. The hydrodynamic lubrication of rough bearing surfaces of finite width. *J Lubric Tech-T ASME* 1971; 93: 324–329.
20. Tonder K and Christensen H. Waviness and roughness in hydrodynamic lubrication. *Proc Inst Mech Eng* 1972; 186: 807–812.
21. Tonder K. Lubrication of surfaces having area-distributed isotropic roughness. *J Lubric Tech-T ASME* 1977; 99: 323–330.
22. Rhow S and Elrod H. The effects on bearing load-carrying capacity of two-sided striated roughness. *J Lubric Tech-T ASME* 1974; 96: 554–560.
23. Rohde S and Whicker D. Some mathematical aspects of the hydrodynamic lubrication of rough surfaces. In: *Surface roughness effects in lubrication: proceedings of the 4th Leeds–Lyon symposium on tribology*, Lyon, 1977.
24. Sun D. On the effects of two-dimensional Reynolds roughness in hydrodynamic lubrication. *P Roy Soc A-Math Phy* 1978; 364: 89–106.
25. Patir N and Cheng H. An average flow model for determining effects of three-dimensional roughness on partial hydrodynamic lubrication. *J Lubric Tech-T ASME* 1978; 100: 12–17.
26. Patir N and Cheng H. Applications of average flow model for determining effects of three-dimensional roughness on partial hydrodynamic lubrication. *J Lubric Tech-T ASME* 1979; 101: 220–230.
27. Tripp J. Surface roughness effects in hydrodynamic lubrication: the flow factor method. *J Lubric Tech-T ASME* 1983; 105: 458–465.
28. Kistler A, Cheng H, Nivatvongs K, et al. Cavitation phenomenon in face seals. ONR Contract N00014-79-0007, 1980.
29. Harp S and Salant R. Surface lubrication with interasperity cavitation. *J Tribol-T ASME* 2001; 123: 134–143.
30. Almqvist A, Lukkassen D, Meidell A, et al. New concepts of homogenization applied in rough surface hydrodynamic lubrication. *Int J Eng Sci* 2007; 45: 139–154.
31. Phan-Thien N. Hydrodynamic lubrication of rough surfaces. *P Roy Soc A-Math Phy* 1982; 383: 439–446.
32. Bayada G and Faure J. Double scale analysis approach of the Reynolds roughness comments an application to the journal bearing. *J Tribol-T ASME* 1989; 111: 323–330.
33. Buscaglia G and Jai M. Homogenization of the generalized Reynolds equation for ultra-thin gas films and its resolution by FEM. *J Tribol-T ASME* 2004; 126: 547–552.
34. Kane M and Bou-Said B. Comparison of homogenization and direct techniques for the treatment of roughness in incompressible lubrication. *J Tribol-T ASME* 2004; 126: 733–737.
35. Sahlin F, Almqvist A, Larsson R, et al. Rough surface flow factors in full film lubrication based on a homogenization technique. *Tribol Int* 2007; 40: 1025–1034.
36. Bayada G, Martin S and Vazquez C. Micro-roughness effects in (elasto)hydrodynamic lubrication including a mass-flow preserving cavitation model. *Tribol Int* 2006; 39: 1707–1718.
37. Szeri A. *Fluid film lubrication*. New York: Cambridge University Press, 2011.
38. Mate C. *Tribology on the small scale*. New York: Oxford University Press, 2008.
39. Hu Y and Tonder K. Simulation of 3-D random rough surface by 2-D digital filter and Fourier analysis. *Int J Mach Tool Manu* 1992; 32: 83–90.
40. Lacey C and Talke F. A tightly coupled numerical foil bearing solution. *IEEE T Magn* 1990; 26: 3039–3043.
41. Hirsch C. *Numerical computation of internal and external flows: fundamentals of computational fluid dynamics*, 2nd edn. Oxford: Butterworth-Heinemann, 2007.
42. Bronshtein I, Semendyayev K, Musiol G, et al. *Handbook of mathematics*, 5th edn. Berlin: Springer, 2007.

43. Etsion I, Kligerman Y and Halperin G. Analytical and experimental investigation of laser-textured mechanical seal faces. *Tribol T* 1999; 42: 511–516.
44. Kweh C, Patching M, Evans H, et al. Simulation of elastohydrodynamic contacts between rough surfaces. *J Tribol-T ASME* 1992; 114: 412–419.
45. Venner C and Napel W. Surface roughness effects in an EHL line contact. *J Tribol-T ASME* 1992; 114: 616–622.
46. Zhu D and Ai X. Point contact EHL based on optically measured three-dimensional rough surfaces. *J Tribol-T ASME* 1997; 119: 375–384.
47. Elrod H. A general theory for laminar lubrication with Reynolds roughness. *J Lubric Tech-T ASME* 1979; 101: 8–14.
48. Phan-Thien N. On the effects of the Reynolds and Stokes surface roughnesses in a two-dimensional slider bearing. *P Roy Soc A-Math Phy* 1981; 377: 349–362.
49. Bayada G and Chambat M. New models in the theory of the hydrodynamic lubrication of rough surfaces. *J Tribol-T ASME* 1988; 110: 402–407.
50. Arghir M, Roucou N, Helene M, et al. Theoretical analysis of the incompressible laminar flow in a macro-roughness cell. *J Tribol-T ASME* 2003; 125: 309–318.
51. Almqvist T and Larsson R. Some remarks on the validity of Reynolds equation in the modeling of lubricant film flows on the surface roughness scale. *J Tribol-T ASME* 2004; 126: 703–710.
52. Phan-Thien N. On the effect of parallel and transverse stationary random surface roughness in hydrodynamic lubrication. *P Roy Soc A-Math Phy* 1981; 374: 569–591.
53. Feldman Y, Kligerman Y, Etsion I, et al. The validity of the Reynolds equation in modeling hydrostatic effects in gas lubricated textured parallel surfaces. *J Tribol-T ASME* 2006; 128: 345–350.
54. Ausas R, Ragot P, Leiva J, et al. The impact of the cavitation model in the analysis of microtextured lubricated journal bearings. *J Tribol-T ASME* 2007; 129: 868–875.
55. Dobrica M, Fillon M, Pascovici M, et al. Optimizing surface texture for hydrodynamic lubricated contacts using a mass-conserving numerical approach. *Proc IMechE, Part J: J Engineering Tribology* 2010; 224: 737–750.

Appendix

Notation

A	amplitude of the sinusoidal roughness
c	minimum bearing spacing
f	bearing friction coefficient, $f = F_f/(WS)$
f_c	cutoff frequency of the low-pass filter to generate the isotropic random roughness
f_s	sampling frequency of the low-pass filter to generate the isotropic random roughness
F_f	non-dimensional friction force between the sliding bearing surfaces
$h(x,y)$	local bearing spacing
h_p	dimple depth
$H(X,Y)$	non-dimensional local bearing spacing, $H(X,Y) = h(x,y)/c$
k	wave number of the sinusoidal roughness
N	number of dimples in the dimple column of the textured bearing
$p(x,y)$	local bearing gauge pressure
p_0	atmospheric pressure
$P(X,Y)$	non-dimensional local bearing gauge pressure, $P(X,Y) = p(x,y)/p_0$
q	volume flow rate of the bearing
Q	non-dimensional volume flow rate of the bearing, $Q = q/(Ur_pc/2)$
r_p	dimple radius
r_1	half edge length of a square unit cell in the textured bearing
R	surface height of the sinusoidal roughness
S	non-dimensional bearing area
S_p	texture density, $S_p = \pi r_p^2/(4r_1^2)$
U	relative sliding speed of the textured parallel slider bearing
W	non-dimensional bearing load-carrying capacity per unit area
x, y, z	Cartesian coordinates
X, Y, Z	non-dimensional Cartesian coordinates, $X = x/r_p$, $Y = y/r_p$, $Z = z/c$
α	normalized frequency of the isotropic random roughness with Gaussian distribution of surface heights, $\alpha = f_c/f_s$
δ	non-dimensional minimum bearing spacing, $\delta = c/2r_p$
ε	texture aspect ratio, $\varepsilon = h_p/2r_p$
λ	flow parameter, $\lambda = 3\mu U/2r_p p_0$
μ	lubricant dynamic viscosity
σ	root mean square (RMS) roughness
σ^*	non-dimensional RMS roughness, $\sigma^* = \sigma/h_p$
τ_{zx}	shear stress on the smooth surface in the flow direction (x-direction)
T_{ZX}	non-dimensional shear stress on the smooth surface in the flow direction (X-direction)
φ	phase of the sinusoidal roughness
Ω	textured bearing domain